

Radio variability of the gamma-ray blazar 0202+149

T.B. Pyatunina¹, S.G. Marchenko^{2,3}, A.P. Marscher³, M.F. Aller⁴, H.D. Aller⁴, H. Teräsranta⁵, and E. Valtaoja⁶

¹ Institute of Applied Astronomy, Zhdanovskaya St. 8, 197110 St. Petersburg, Russia (ptb@ipa.rssi.ru)

² Astronomical Institute, St. Petersburg State University, Bibliotechnaya pl. 2, 198904 St. Petersburg, Russia

³ Institute for Astrophysical Research, Boston University, 725 Commonwealth Ave., Boston, MA 02215, USA

⁴ Astronomy Department, University of Michigan, Ann Arbor, MI 48109, USA

⁵ Metsähovi Radio Research Station, Helsinki University of Technology, 02540 Kylmälä, Finland

⁶ Tuorla Observatory, University of Turku, 21500 Piikkiö, Finland

Received 23 April 1999 / Accepted 11 February 2000

Abstract. Analysis of radio light curves of the γ -ray bright blazar 0202+149 at frequencies of 37, 22, 14.5, 8, and 4.8 GHz during the period 1984–1998 reveals a 4-year cycle of variability with substructure on a shorter time scale of about 1.3-yr. The 4.8–37 GHz spectral index of the source gradually increases from -0.04 ($T=1990.2$) to 0.4 ($T=1996.6$) and during outbursts shows strong variations with a time scale of about 1 year and an amplitude up to ~ 0.4 . VLBI images at 8, 22, and 43 GHz show a core-dominated structure with a faint jet in the northwest direction, which we trace out to 7 mas, with a bent inner part ($r \leq 1$ mas) consisting of at least 2 components. The connection of the jet activity with the 4-year cycle of total flux density variability is discussed.

Key words: galaxies: active – galaxies: quasars: individual: 0202+149 – radio continuum: galaxies

1. Introduction

The quasar 0202+149 has an optical spectrum with narrow emission lines typical of low to moderate ionization narrow line radio galaxies (Stickel et al. 1996). There are a few very different estimates of its redshift: $z = 0.405$ in NED, $z = 1.202$ (Comastri et al. 1997) and $z = 0.833$ (Stickel et al. 1996). Since the latter authors derived the redshift from emission lines that they were able to detect, we consider their determination as the most reliable. At optical wavelengths the source has been imaged by Peacock et al. (1981), who find it to be faint and point-like ($m_R=21.3$, Stickel et al. 1996; $m_V=20.9$, Impey & Tapia 1990). The photometric colors in the visible range point to a power law $S_\nu \propto \nu^{-\alpha}$ with index $\alpha=2.3$ (Fughmann & Meisenheimer 1988). The infrared measurements show very large variations by a factor of ~ 8 in 1 month and give a power law with $\alpha=2.5$, both when the source is faint and when it is bright (Stickel et al. 1996). Therefore, the optical and infrared spectra are consistent with each other, although the measurements are not simultaneous. A fairly high level of optical polarization ($p_{max}=4\%$) was

found by Impey & Tapia (1990). The quasar 0202+149 was detected by EGRET as a γ -ray source (von Montigny et al. 1995) and classified as a variable source with a high level of probability in the second EGRET catalog (Mattox et al. 1997). In the radio band 0202+149 is classified as a flat-spectrum radio source, with mean spectral index in the region from 400 MHz to 8 GHz equal to $\alpha=0.33$ (Herbig & Readhead 1992) and average flux density at 5 GHz of ~ 2.7 Jy.

All the aforementioned features of the quasar 0202+149 make it an interesting object for investigation of its detailed VLBI structure. We present geodetic centimeter-wave VLBI observations and high dynamic range millimeter-wave VLBA observations, which, together with the results of more than 20 years monitoring of the flux density at centimeter wavelengths carried out at the University of Michigan Radio Astronomy Observatory (UMRAO, Aller et al. 1985) and at millimeter wavelengths at Metsähovi Radio Research Station (Teräsranta et al. 1992), should allow us to relate individual events to provide a coherent scenario of the source variability.

2. Observations and reduction

2.1. (a) Geodetic VLBI data

We have used in this work 8 GHz geodetic data obtained with the Global VLBI Network at 8 epochs during the period from 1995.06 to 1996.68. All the data have been received from Goddard Space Flight Center. Calibration parameters necessary for conversion of the correlation coefficients into correlated flux densities were kindly provided by Dr. D. Shaffer. Mapping and model-fitting with elliptical gaussian components were performed with the Caltech VLBI Package software on a VAX634 computer.

2.2. (b) 22 and 43 GHz VLBA observations

We observed 0202+149 with the VLBA as a part of a γ -ray bright blazar monitoring campaign at 5 epochs between 1994.18 and 1997.58 at frequencies of 22 and 43 GHz. The observations were carried out with the VLBA recording system using four

Send offprint requests to: T.B. Pyatunina

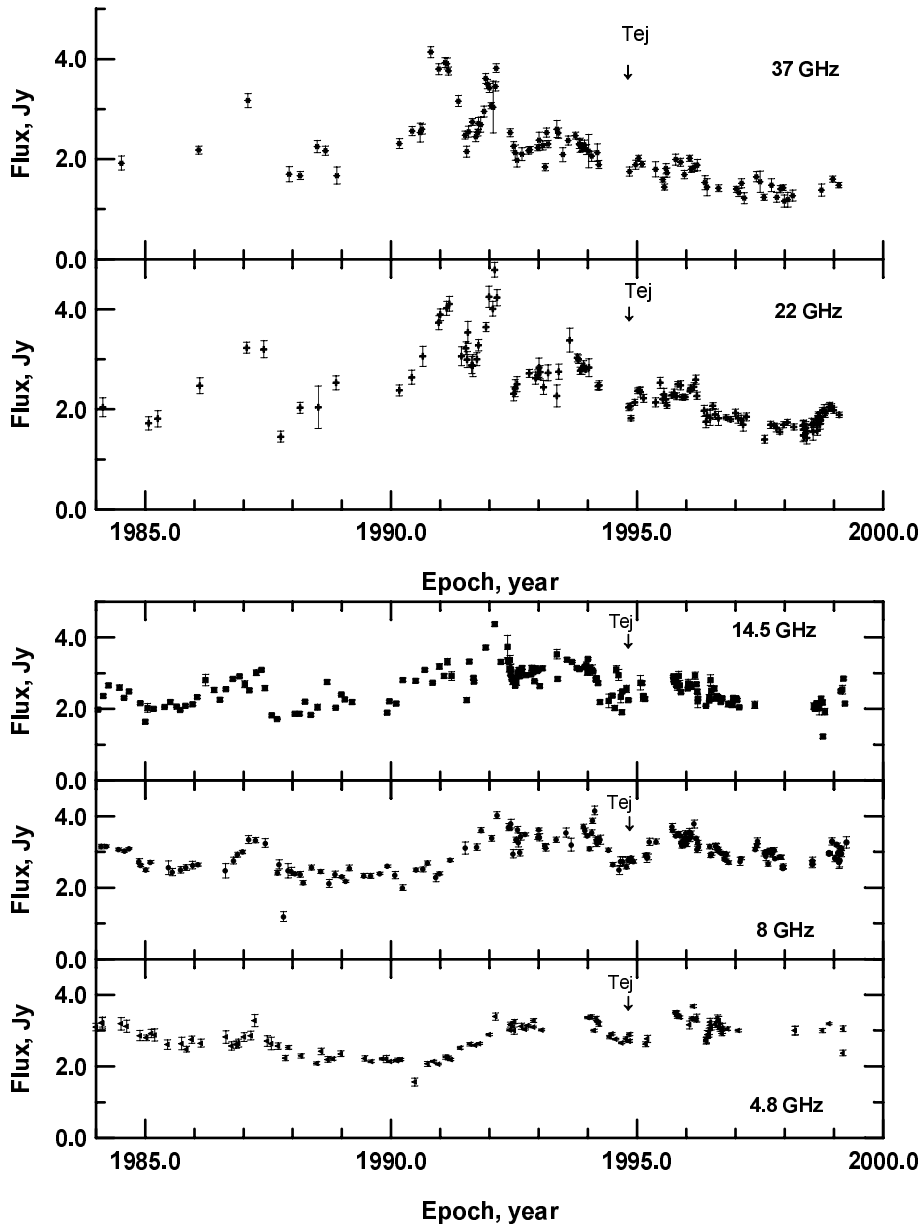


Fig. 1. The total flux density of 0202+149 as a function of time

8 MHz wide channels in both right and left circular polarization, in “snapshot” mode. The flux densities were calibrated using 22 and 37 GHz single-antenna measurements obtained at the Metsähovi Radio Research Station. Corrections were made for zenith opacities, antenna gain curves, and system temperatures (the latter two supplied by NRAO).

The Astronomical Image Processing System (AIPS) software was used for primary data reduction, while imaging and model fitting were performed as above but using the software Difmap (Shepherd 1997). The flux densities were adjusted a posteriori for discrepancies between the gain curves and actual antenna performance by requiring that the total fluxes on the images of nearly unresolved calibrating sources match the Metsähovi values.

3. Time scales of the radio variability

3.1. Visual inspection

We analyse the radio light curves of 0202+149 at 37 and 22 GHz (Fig. 1 top) obtained in 1984–1998 with the 13.7 m telescope at Metsähovi and at 14.5, 8.0 and 4.8 GHz (Fig. 1 bottom) from the 26 m telescope at UMRAO during the same period. The total flux density of the source shows complex variability over a wide range of time scales from as short as ~ 1 year to longer than 10 years; short timescale variations dominate at mm wavelengths, while longer timescales are prominent at cm wavelengths.

Close inspection of the mm-wave total flux density curves suggests the possibility of a periodicity on a timescale of about 4 years. Fig. 2 presents three 4-year cycles of the flux variability

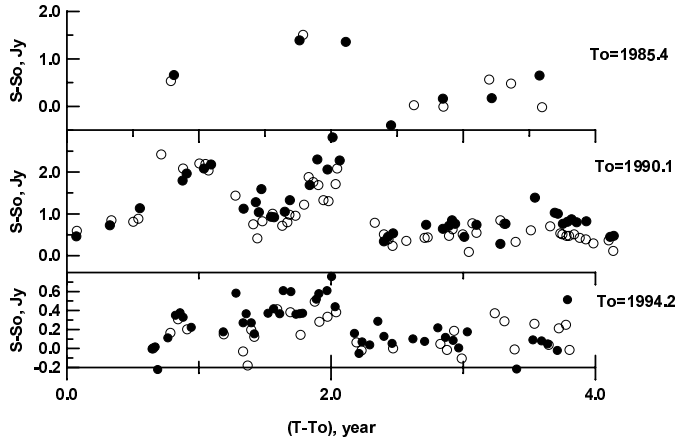


Fig. 2. Light curves separated into three 4-year cycles at 22 (open circles) and 37 (solid circles) GHz after subtraction of the long-term trend.

at 22 and 37 GHz when the long-term trend S_o (see below) is subtracted from the flux density S . The top panel gives the first cycle (C1), which starts at $T_o=1985.3$ (the data are very sparse). The middle and bottom panels show the second (C2, $T_o=1990.1$) and the third (C3, $T_o=1994.2$) cycles.

All three cycles display a similar structure of variability, with global maxima near the middle of the period, despite the fact that the 1996 outburst is nearly 5 times fainter than two previous outbursts. Fig. 2 shows that the 4-year cycle probably consists of two parts: a bright first half (“outburst”) with two maxima (~ 1991 and ~ 1992 , in cycle C2, labeled below in Fig. 3 as I and II, respectively, and ~ 1995 and ~ 1996 , in cycle C3, labeled as 1 and 2) and more quiescent second half (“post-outburst”) with very faint maximum (~ 1988.7 , in cycle C1; ~ 1993.7 , in cycle C2, labeled as III; ~ 1997.7 , in cycle C3, labeled as 3). The time between the outbursts is 4.4 ± 0.4 yr. Taking into account this estimate, we can expect a new maximum at mm wavelengths near ~ 1999.0 ; the 22 GHz total flux density curve (Fig. 1) does show a maximum at this epoch quite clearly. Some indications of the maximum are seen also at 14.5 and 8 GHz.

Fig. 3 shows cycles C2 and C3 at all frequencies from 37 to 4.8 GHz after subtraction of the long-term trend (see below under time series analysis). The main maximum of a cycle (denoted as II in cycle C2 and as 2 in cycle C3) takes place at all the frequencies almost simultaneously and has a rather flat spectrum (see Sect. 3.2). On the contrary, the preceding maximum (denoted as I and 1, respectively, in cycles C2 and C3) is delayed by approximately 0.7 ± 0.1 yr at 4.8 and 8 GHz relative to 14.5, 22 and 37 GHz. Whereas in cycle C2 this maximum is most prominent at 22 and 37 GHz, in cycle C3 it is much higher at 8 GHz.

3.2. Evolution of the total flux density spectrum

We construct the spectral energy distribution in the range from 4.8 to 37 GHz for several similar phases of cycles C1, C2, and C3 (Fig. 4), where the phase is a duration in years from the start point of the cycle. The figure shows that the overall spectrum

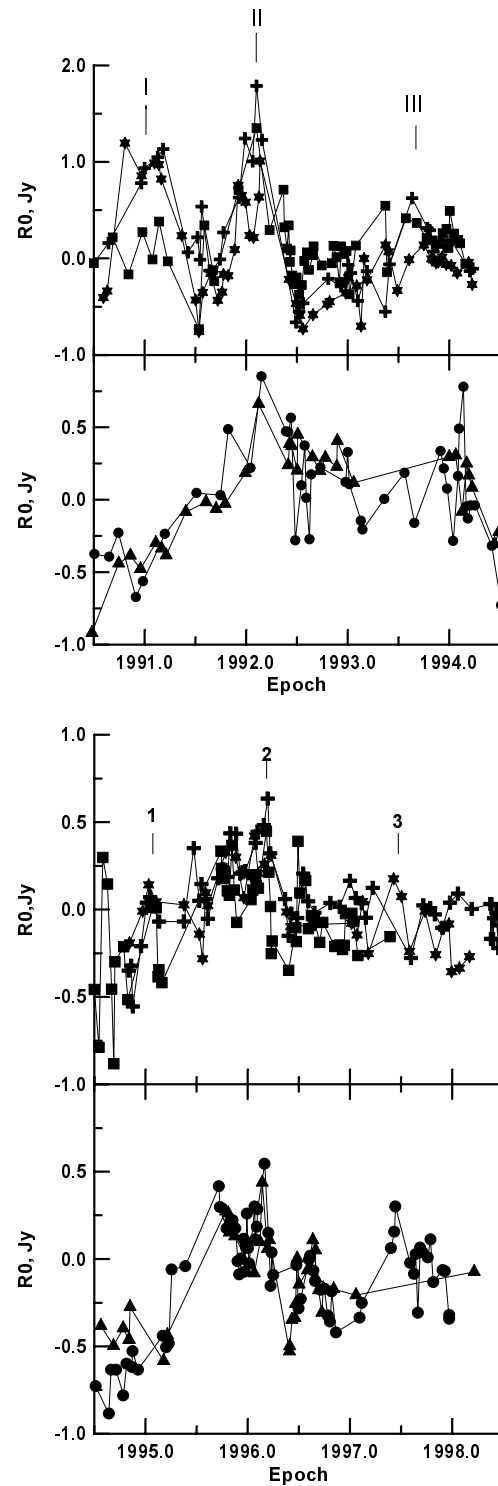


Fig. 3. Flux densities at frequencies 37 (asterisks), 22 (crosses), 14.5 (squares), 8 (circles) and 4.8 (triangles) GHz after removing the long-term trend for cycles C2 (top) and C3 (bottom).

steepened from cycle C1 to cycle C3 and that the turnover frequency evolved from 37 to 8 GHz, respectively. Fig. 4 demonstrates a difference between the spectra at the two maxima of cycle C2 (I - corresponding to $T - T_o \sim 1.0$ and II - correspond-

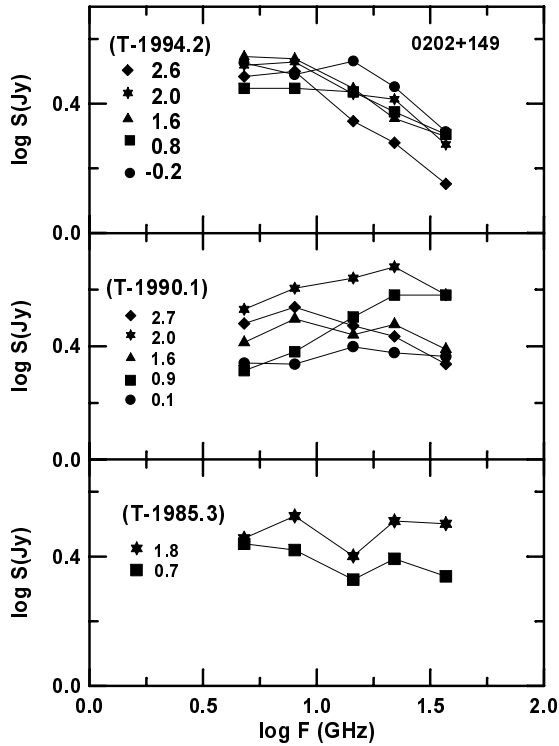


Fig. 4. Spectra of the total flux density over the range 4.8 to 37 GHz in cycles C1(bottom), C2(middle), and C3 (top).

ing to $T - T_o \sim 2.0$). The spectrum at maximum I peaked at 37 GHz and steeply declined to 8 GHz, while the spectrum at maximum II was rather flat and peaked at 22 GHz.

In order to separate the spectra of outbursts from the spectra of the long-term components, we subtracted from the flux densities at maxima I and II the average values of flux densities just before and after the corresponding outbursts. The spectra obtained are presented in Fig. 5; these show that the turnover frequency at maximum I is ≥ 37 GHz while at maximum II it is close to 22 GHz. The spectral indexes ($S_\nu \propto \nu^{-\alpha}$) for the frequency range of the spectra from 8 to 22 GHz are $\alpha = -2.1$ to -1.1 for the I and II maxima correspondingly. The spectral index for the optically thin part of the spectra at maximum II can be estimated as $\alpha \leq 0.43$. The spectral index of optically thin part of spectrum at maximum I can't be estimated due to lack of data above 37 GHz. Unfortunately, analogous estimates for maxima 1 and 2 in cycle C3 are rather uncertain due to the low flux densities of the outbursts at high frequencies. It is interesting to point out that the spectrum at epoch T=1991.7 (the intermediate between the two maxima) has two humps, at frequencies 8 and 22 GHz.

3.3. Time series analysis

To confirm our visual estimate of the characteristic time scales of the radio variability of 0202+149 we performed a time series analysis of the radio light curves and array of spectral indices in the range of 4.8 – 37 GHz, using two methods to search

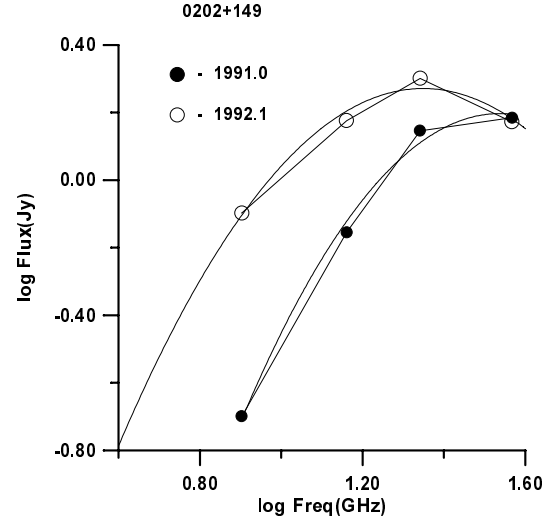


Fig. 5. Spectra of radio emission for outburst components during maxima I (solid circles) and II (open circles). Solid curves show second order polynomial approximation.

for a periodicity - “whitening” (Hagen-Thorn et al. 1997) and CLEAN (Roberts et al. 1987).

The method “whitening” is based on the construction of the periodograms

$$D_{\nu_j} = \frac{1}{N^2} \left| \sum_{k=1}^N x(t_k) \exp(-i2\pi\nu_j t_k) \right|^2,$$

where $i^2 = -1$, $x(t_k)$ is the initial time series with the mean flux density subtracted, N is the total number of points, and ν_j is the array of frequencies. The periodograms are constructed for residual time series formed by the successive subtraction of a sinusoidal component corresponding to the maximum periodogram value of the previous series. Subtraction of the long-term harmonics (the period of the harmonic is longer than half of the total duration of observations) removes the underlying long-term trend. Fig. 6a presents the first periodogram of the initial light curve at 4.8 GHz, which has a primary maximum at a frequency corresponding to 13.7 ± 1.1 years. The first periodograms for other light curves have the same form and show the presence of long-term trends with characteristic time scales in the range 11-14 years (The CLEAN method gives similar results, see Table 1). Fig. 6b shows a fit between the data at 4.8 GHz and the long-term trend.

For all light curves, the functions of the spectral window were constructed. As an example, Fig. 7a presents the function of the spectral window at 22 GHz, where labels *A*, *B* and *C* mark the maxima at frequencies $\nu=0.00055 \pm 0.00002$ (5-year harmonic), $\nu=0.00115 \pm 0.00001$ (2-year harmonic), and $\nu=0.00280 \pm 0.00001$ (1-year harmonic) caused by unequally spaced data that generate aliases in the power spectra. The aliases, which usually appear in pairs on either side of “real” peaks in the power spectra, are labeled by a letter with a number, where the letter corresponds to a peak in a spectral window (see

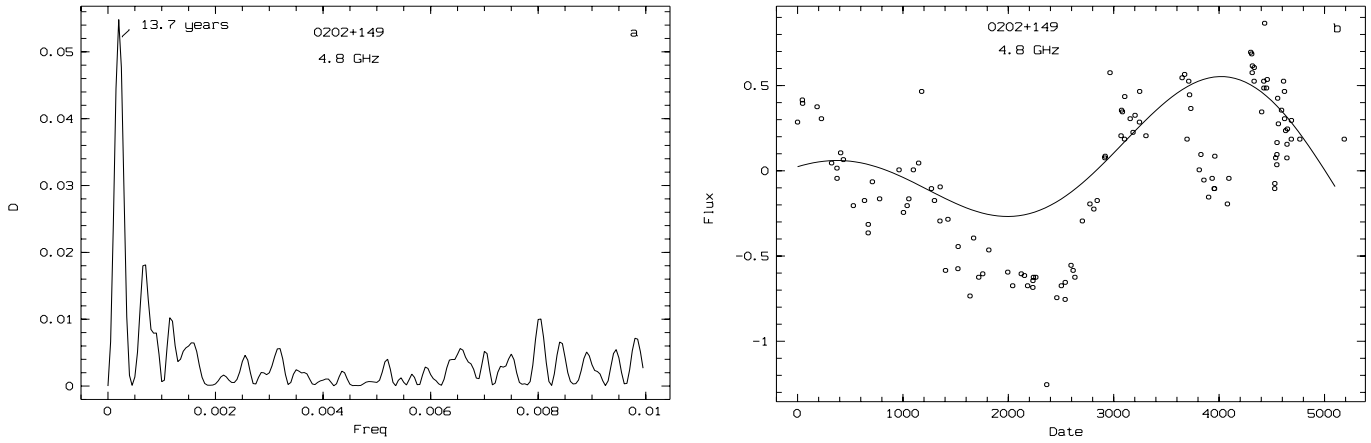


Fig. 6. Long-term trend of the flux variability at 4.8 GHz: a) the first periodogram of the original light curve at 4.8 GHz; b) comparison of the flux densities at 4.8 GHz (circles; the average value of the flux density is subtracted) with the long-term trend (solid curve), obtained as a sum of the 13.7- and 11.1-year harmonics that give the main maxima in the first and second periodograms.

Fig. 7a) and the number is the modulus of the corresponding period found in the data.

We subtract the long-term trends approximated by the sum of (usually two) sinusoids (see Fig. 6) from the light curves. Fig. 7 (b–f) present the main periodograms for all frequencies after subtraction of the long-term trend, which, however, is not removed completely (especially at 8.0 GHz, where the CLEAN method indicates the presence of the most complicated long-term trend; see Table 1), but whose influence is decreased sufficiently to study shorter characteristic time scales of variability.

The analysis of the periodograms shows that the light curves have a typical time scale of variability of $P \sim (4.2 \pm 0.8)$ yr (at 8 GHz the most prominent harmonic, 3.2 ± 0.6 yr, is within the 2σ -uncertainties of the 4-year harmonic). The 4-year cycle has substructures with typical timescales of 2.3 ± 0.2 yr and 1.3 ± 0.1 yr. The 1.3 ± 0.1 yr scale is more pronounced in the 37 and 22 GHz periodograms, while the 4.8, 8.0, and 14.5 GHz periodograms show the 2.3 ± 0.2 yr timescale.

Parameters of harmonics found by the CLEAN method are given in Table 1 (the first column gives the frequency of the analysed light curve; the second column, the period of each harmonic P ; the third column, the amplitude of each harmonic A ; and the fourth column, the phase of each harmonic Φ). The table contains the harmonics that exceed the level of noise, defined at every frequency by the formula: $noise = \frac{\bar{D} * Xq}{1 + sn}$, where \bar{D} is the mean value of the power spectrum, sn is the ratio of the standard deviation of a single observation to the error of a single measurement, $Xq = -\ln(1 - \exp((\frac{2}{N-2})\ln(Pr)))$, where Pr is the level of significance. A comparison of Fig. 7 and Table 1 shows that the results of analysis by the CLEAN and “whitening” methods are in good agreement. Existence of close pairs of harmonics (13.7 & 11.0, 4.6 & 3.0 & 5.5, 2.3 & 1.7 years) can be easily explained by deviations from strict periodicity, namely, by amplitude modulations and phase delays at different frequencies.

It is noteworthy that the light curves of 0202+149 at 318, 430, 660, 880, and 1400 MHz obtained during a 5-year

Table 1. Parameters of harmonics found by CLEAN method

Freq GHz	P year	A Jy	Φ rad
4.8	13.7	0.250	0.799
	11.0	0.087	0.229
	4.6	0.051	0.671
	2.9	0.016	6.076
	1.7	0.028	0.620
8.0	54.8	0.024	3.314
	13.7	0.173	1.632
	11.0	0.087	0.779
	4.6	0.021	1.434
	3.0	0.065	0.602
	2.3	0.045	4.725
14.5	1.7	0.038	1.400
	13.7	0.124	2.491
	11.0	0.178	1.447
	5.5	0.024	2.808
	2.3	0.061	5.075
	1.8	0.011	2.306
22	0.9	0.006	2.926
	13.7	0.201	3.023
	11.0	0.329	1.915
	4.2	0.055	1.889
	2.3	0.054	4.606
	1.2	0.057	3.432
37	0.8	0.043	1.276
	11.0	0.538	2.464
	4.2	0.089	2.718
	1.3	0.085	6.108
	0.9	0.028	5.937

program of multifrequency monitoring by Mitchell et al. (1994) over the period 1980–1985 reveal the possible presence of a similar 4-year cycle starting between the end of 1980 and beginning of 1981. The recently published long-term light curves

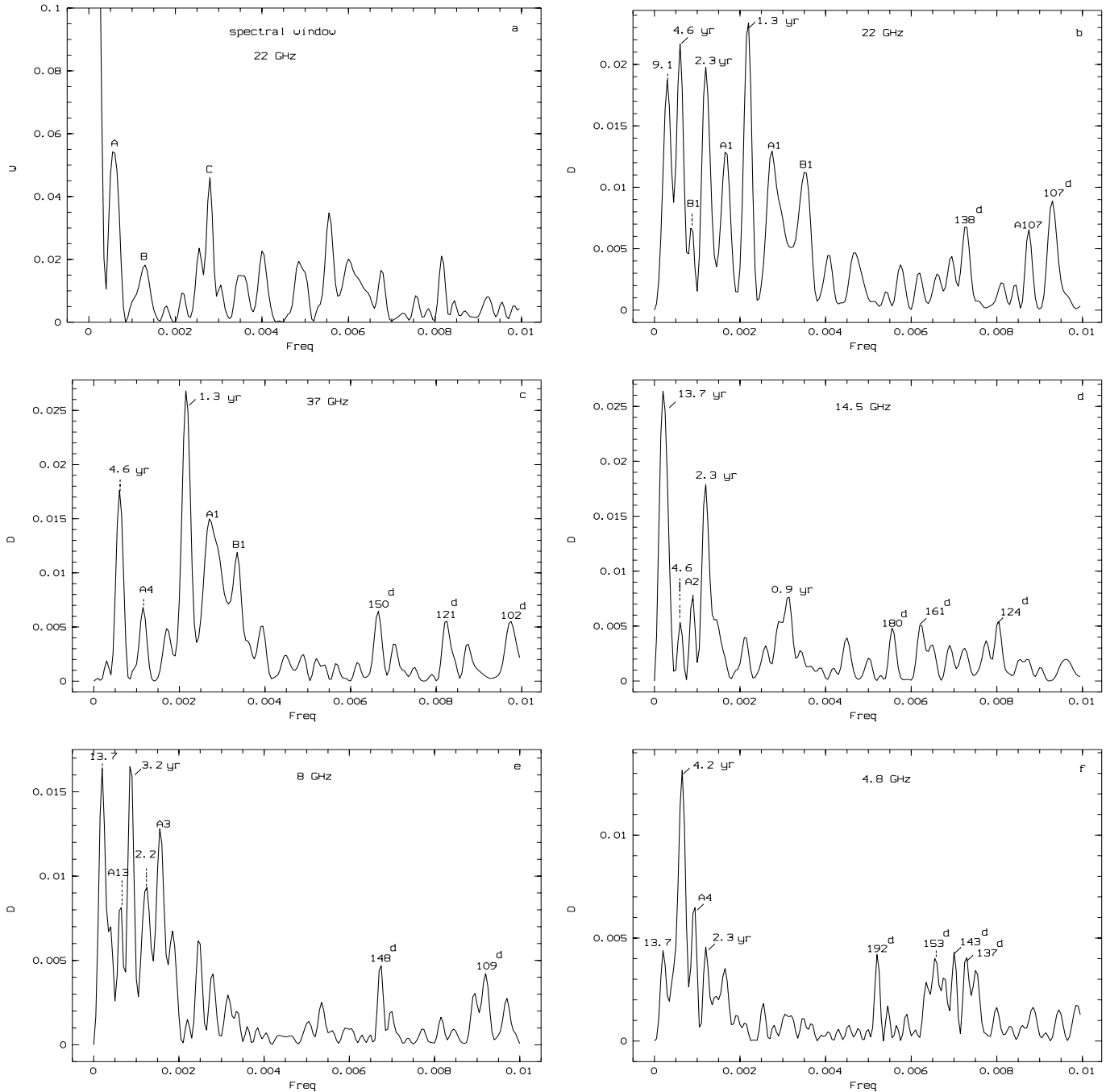


Fig. 7. Time series analysis: a) the function of the spectral window for the observational grid at 22 GHz; b–f) the periodograms of the 0202+149 light curves after subtraction of the long-term trend at 22, 37, 14.5, 8.0, and 4.8 GHz, respectively.

at 318 and 430 MHz based on the Arecibo measurements (Salgado et al.1999) seem to show a variability on the timescale ~ 13 yr.

3.4. Evolution of the spectral index

We construct the array of spectral indices of 0202+149 in the radio region from 4.8 GHz to 37 GHz, considering that observations at different frequencies are simultaneous if the difference

between dates of observations does not exceed 0.05 yr. The values of spectral indices α ($S \propto \nu^{-\alpha}$) estimated by the least-squares method are given in Fig. 8a. The figure shows a gradual steepening of the spectrum of the source from 1990 to 1998 that corresponds to a long-term trend of variability with time scale ~ 11 yr and amplitude 0.35 ± 0.06 .

The time series analysis of the array after subtraction of the long-term trend reveals the presence of a 4-year cycle of spectral index variability with amplitude 0.08 ± 0.02 (Fig. 8b). This

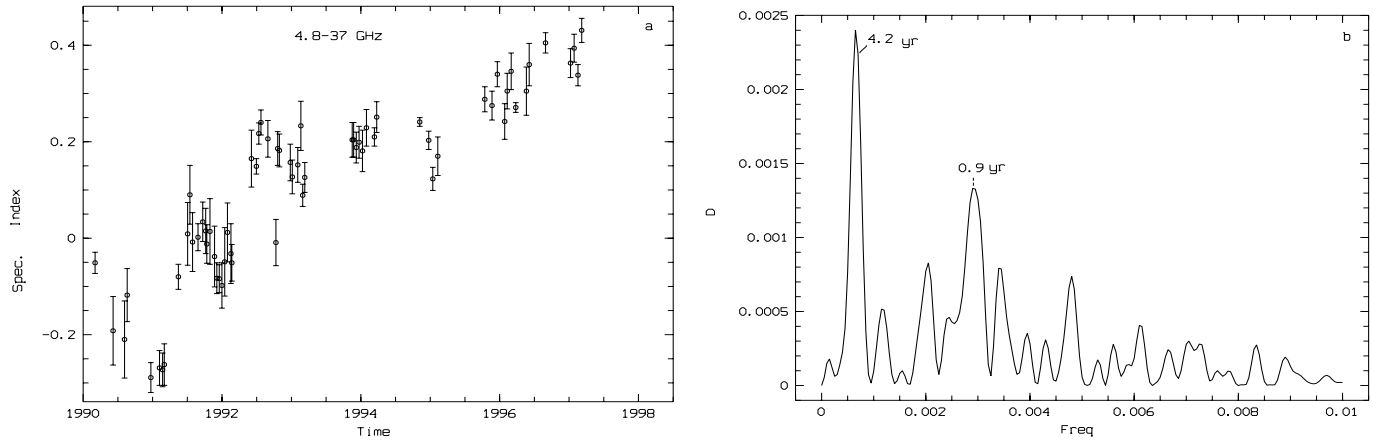


Fig. 8. **a** Spectral index of the total flux density in the range from 4.8 to 37 GHz versus time; **b** the periodogram of the spectral index array after subtraction of the long-term trend.

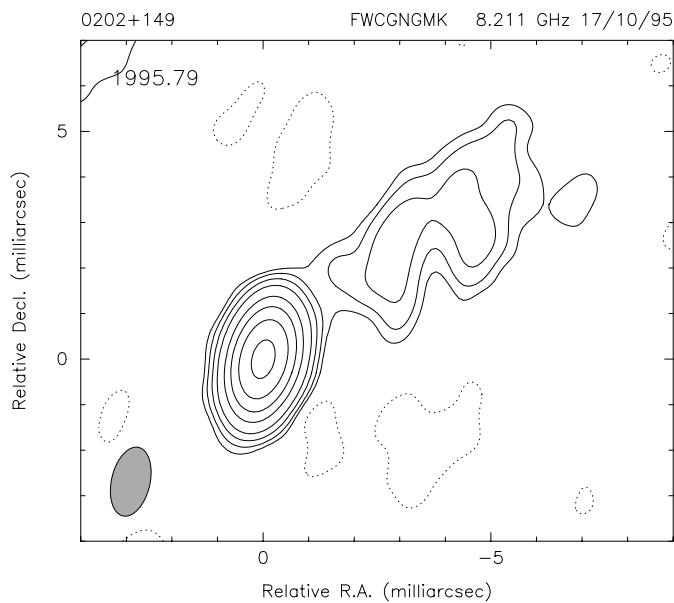


Fig. 9. A tapered map of 0202+149 at 8 GHz; the contours start at level 0.5% and increase by factors of 2; the map peak is 2.04 Jy/beam.

is further confirmation that a 4-year cycle is the most characteristic time scale of the flux density variations at mm- and cm-wavelengths. The periodogram in Fig. 8b also shows a 1-year time scale of variability. The amplitude of the variations reaches ~ 0.4 near 1991 and significantly decreases after 1993.

4. Structure of the VLBI jet

4.1. Outer jet structure

A map of 0202+149 at 8 GHz, tapered by down-weighting the long-baseline data, shown in Fig. 9, reveals a core-dominated structure with a faint, quasi-linear jet extending out to ~ 7 mas. Our high-dynamic range 22 GHz map (Fig. 10) shows that the more compact part of this diffuse jet is resolved into three components at a distance of 5.2 ± 0.1 mas from the core and at position angle (PA) from -60° to -45° . The structure is similar to

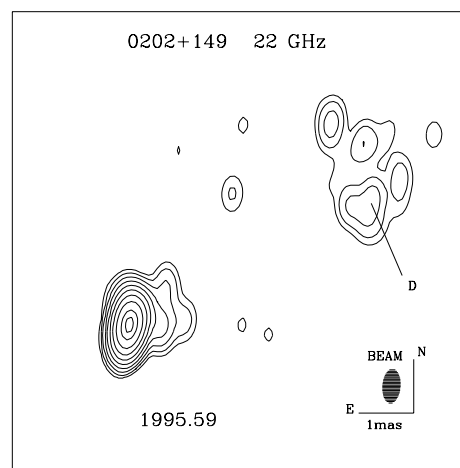


Fig. 10. Hybrid map of 0202+149 at 22 GHz; the contours start at level 0.25% and increase by factors of 2; the map peak is 1.19 Jy/beam.

that of the 15 GHz image of Kellermann et al. (1998). Also, all 43 GHz maps (Table 3) show the presence of a stationary component at a distance of 5.15 ± 0.05 mas at PA $-57^\circ \pm 4^\circ$ (labeled as *D* in Fig. 10). Taking into account the double structure of the inner ($r \leq 1$ mas) region, the jet seems to be resolved in the transverse direction (perhaps with a modest bend), rather than bent by 90° as suggested by Kellermann et al. (1998), although a sharp bend might be present in the inner 1 mas (see below).

4.2. Inner jet structure

For the period from January 1995 to September 1996, more than 10 maps have been obtained from geodetic 8 GHz VLBI observations. The best 8 maps are presented in Fig. 11. We obtained best agreement with observations with a three-component model: a core, labeled as *A*, and two-components (*B* and *C*) of a curved jet. The parameters of the gaussian model components are given in Table 2, where the first column is the epoch of observations, the second designates symbols used for the each component, the third gives the component's flux, the fourth is

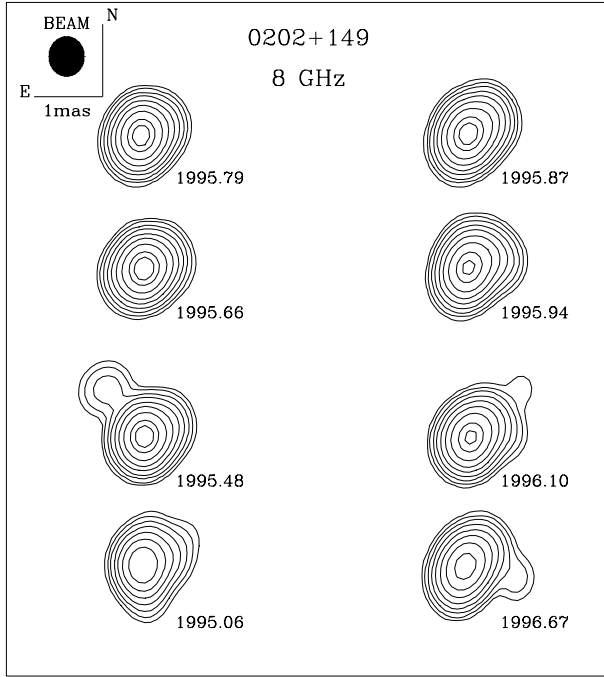


Fig. 11. Hybrid maps of 0202+149 at 8 GHz convolved with a circular Gaussian beam of FWHM similar to the resolution in the direction of the jet as seen in Fig. 9; the contours start at level 0.5% and increase by factors of 2; the map peak is 0.94 Jy/beam in 1996.10.

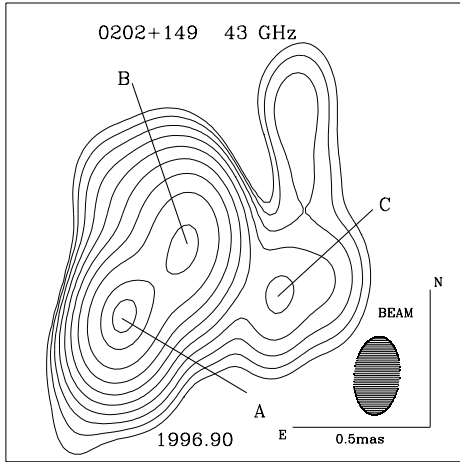


Fig. 12. Hybrid map of 0202+149 at 43 GHz; the contours start at level 0.5% and increase by factors of 2; the map peak is 0.334 Jy/beam.

the distance of the component from the core (R), the fifth, the position angle of the component (Θ), and the sixth, the size of the component (a).

The inner structure of the jet, more clearly seen in the high resolution 43 GHz map (Fig. 12), suggests either strong curvature or complex cross-sectional structure. Hybrid maps at 43 GHz at 4 epochs of observation are shown in Fig. 13. The results of model fitting are summarized in Table 3. The brightest component is designated by the letter *A* and is identified as the core. The size of the core is in the range of 0.05–0.12 mas according to our model fits. The 43 GHz jet consists of at least

Table 2. Model parameters at 8 GHz

Epoch	Comp.	Flux Jy	R mas	Θ deg.	a mas
95.06	A	1.16	0.0	0.0	0.18
	B	0.14	0.47	-64.2	0.0
95.49	A	2.03	0.0	0.0	0.13
	B	0.22	0.52	-76.7	0.0
95.66	A	2.12	0.0	0.0	0.22
	B	0.28	0.39	-70.5	0.0
	C2	0.05	0.93	-72.7	0.0
95.79	A	1.97	0.0	0.0	0.17
	B	0.30	0.37	-58.4	0.0
	C2	0.04	0.83	-85.1	0.47
95.87	A	1.84	0.0	0.0	0.16
	B	0.40	0.38	-56.3	0.0
	C2	0.06	0.80	-90.8	0.0
95.95	A	1.62	0.0	0.0	0.18
	B	0.40	0.36	-54.8	0.0
	C2	0.06	0.73	-85.1	0.0
96.1	A	1.60	0.0	0.0	0.13
	B	0.43	0.35	-55.6	0.0
	C2	0.08	0.79	-81.8	0.0
96.68	A	1.24	0.0	0.0	0.16
	B	0.34	0.35	-51.2	0.0
	C2	0.08	0.84	-85.7	0.73

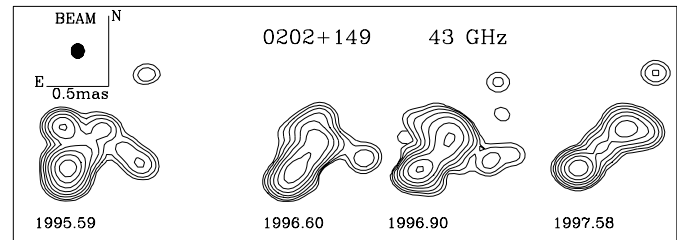


Fig. 13. The hybrid maps of 0202+149 at 43 GHz, convolved with a circular Gaussian beam of FWHM=0.15 mas, similar to the typical resolution along PA -60° ; the contours start at level 0.5% and increase by factors of 2; the map peak is 0.42 Jy/beam in 1995.59

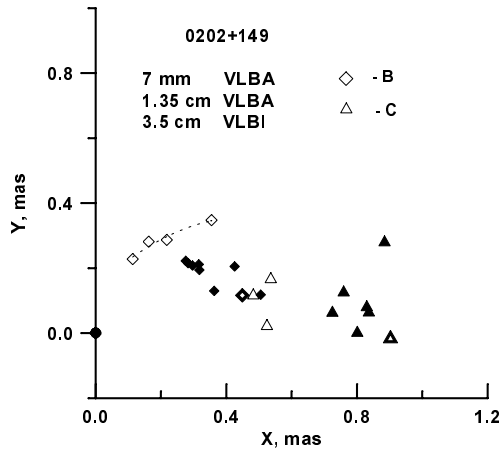
two components, labeled as *B* and *C*. The most distant feature detected at 43 GHz is the aforementioned component *D*, which seems to be stationary.

In Fig. 14 the positions relative to the core *A* of the inner jet components *B* (diamonds) and *C* (triangles) are plotted for 8 GHz (solid), 22 GHz (half-open) and 43 GHz (open). The data at the different frequencies are in reasonable agreement and, taken together, indicate that the trajectories of the components are rather stable.

Displacement between the components at 43 and 8 GHz may correspond to a frequency dependent shift in position of the core due to gradients in opacity (Gómez et al 1997; Lobanov 1998), as suggested also by time delays between the mm- and cm-wave light curves; however, the resolution at 8 GHz is insufficient for a definite conclusion. Fig. 14 shows also that there is a difference of up to 80° in the position angles of the inner jet components,

Table 3. Model parameters at 43 GHz

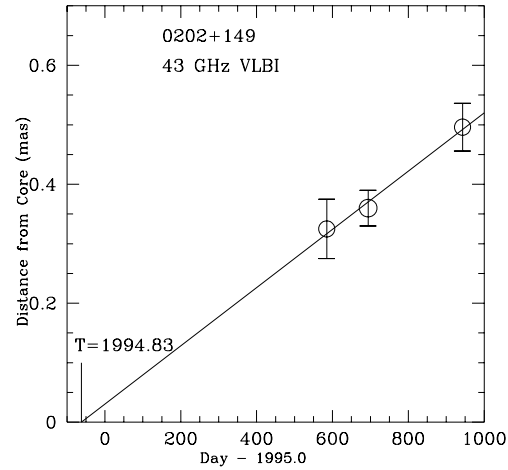
Epoch	Comp.	Flux Jy	R mas	Θ deg.	a mas
95.59	A	0.784	0.0	0.0	0.05
	B1	0.267	0.254	-26.4	0.15
	B2	0.125	0.359	8.7	0.0
	C	0.062	0.496	-76.6	0.16
	D	0.064	5.12	-60.4	0.65
96.60	A	0.689	0.0	0.0	0.12
	B	0.386	0.325	-30.0	0.12
	C	0.038	0.561	-72.9	0.19
	D	0.062	5.17	-57.5	0.82
96.90	A	0.594	0.0	0.0	0.11
	B	0.605	0.360	-37.2	0.17
	C	0.028	0.525	-87.7	0.0
	D	0.020	5.13	-58.7	0.40
97.58	A	0.438	0.0	0.0	0.07
	B3	0.086	0.261	-42.8	0.10
	B+C	0.396	0.496	-45.6	0.13
	D	0.031	5.17	-50.8	0.46

**Fig. 14.** Rectangular coordinates of components *B* (diamonds) and *C* (triangles) at 43 (open), 22 (half-open) and 8 (solid) GHz relative to the core.

which could be explained by strong curvature of the inner jet. The presence of stationary component *D* at a distance ~ 5.2 mas and PA $\sim -60^\circ$ suggests that the jet wiggles through one more turn of a few tens of degrees toward its initial direction beyond 1 mas from the core. The 8 GHz (and 22 GHz) component *B* is resolved on the 43 GHz map into components *B* and *C*. The 8 GHz (and 22 GHz) component *C* is not seen at 43 GHz, probably due to a low surface brightness. Despite fluctuations in the position of component *C*, it is also rather stationary.

5. Superluminal motion

The 8 GHz data allow us to set only an upper limit on the apparent motion of component *B*: $\mu \leq 0.2$ mas/yr (Pyatunina 1998). However, the higher resolution 43 GHz data do reveal motion

**Fig. 15.** Relative separation at 43 GHz of component *B* from the core versus time.

of component *B* as shown in Fig. 15, which presents the separation of component *B* from the core as a function of time. There is no evidence in the data for non-linear motion within the time interval from 1996.6 to 1997.6 despite the strong bend of the inner jet. A linear fit to the data yields an apparent angular separation rate of $\mu = 0.18 \pm 0.01$ mas/yr, corresponding to an apparent superluminal velocity $v = (8.1 \pm 0.3)c$ ($H_0 = 65$ km s $^{-1}$ Mpc $^{-1}$, $q_0 = 0.1$). Linear back-extrapolation of the motion of *B* gives the time of zero separation as $T_{ej} = 1994.83 \pm 0.06$. This epoch, indicated in Fig. 1, corresponds to the local minimum of the total flux density at all frequencies in cycle C3, which agrees with the results of Mutel et al. (1990) and Krichbaum et al. (1998) that new jet components tend to appear at times of local minima in the light curve of a compact radio source.

6. Flux density variations of the VLBI-components

The flux densities of the compact components as functions of time are shown in Fig. 16, which indicates that at 8 GHz the main maximum in the total flux density curve coincides with the maximum in the core flux and peak 2 with the maximum in the flux of component *B*. Unfortunately, both peaks 1 and 2 at 37 GHz are located within gaps in the VLBA observations at 43 GHz, so we can only follow a slow decline of the core flux density and a possible secondary maximum of the flux density of component *B* between 1996.9 and 1997.58.

7. Discussion

The analysis of the total flux density light curves at mm and cm wavelengths, together with multi-epoch, multi-wavelength VLBI data, allows us to suggest that the 4-year cycle of the total flux density variations is connected with the regular ejection of components with apparent superluminal motion. The VLBI data reveal the existence of a superluminal component (*B*) during cycle C3, with a zero-separation time (from 43 GHz images) close to the beginning of the cycle. Comparison of total flux density variations with variations of the core and the

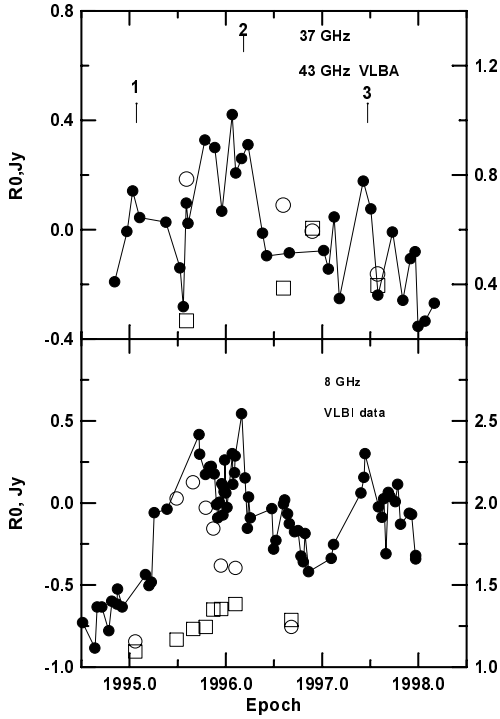


Fig. 16. Relative flux density variations during cycle C3. Filled circles and left y-axis correspond to total flux densities after subtraction of the long-term trend; open symbols and right y-axis correspond to VLBA and VLBI data: open circles - core, squares - component B. 8 GHz component B is shifted up for convenience.

most compact jet component (*B*) allow us to connect the first of the two most prominent outbursts of the aforementioned 4-year cycle (I in cycle C2 and 1 in cycle C3) with the core of the source and the second (II in cycle C2 and 2 in cycle C3) with the jet. According to the total flux density curves (Fig. 1 and also Fig. 16) the outbursts connected with the core show at 8 GHz a time delay (0.7 ± 0.1) yr relative to 37 GHz during both cycles C2 and C3. If we assume that cycles of variability C2 and C3 are distinguished from each other mainly in amplitude and are otherwise similar in physical nature, then we can estimate their physical characteristics by combining the spectral parameters with the estimations of angular sizes and apparent superluminal velocities.

According to Kellermann & Pauliny-Toth (1969) and Marscher (1987) the magnetic field B_{sync} [Gauss] can be estimated from the turnover frequency ν_m [GHz], corresponding flux density S_m [Jy], and angular diameter of the emitting component (approximated as a uniform sphere) at the turnover frequency Θ_{sm} [mas]:

$$B_{sync} = 3.5 \cdot 10^{-5} \Theta_{sm}^4 \nu_m^5 S_m^{-2} \left(\frac{\delta}{1+z} \right).$$

The spherical angular diameter of a component Θ_{sm} can be found from the elliptical gaussian FWHM of the VLBI model fit Θ_{gm} by the relation $\Theta_{sm} = 1.8 \Theta_{gm}$ (Marscher 1987). From

$\beta_{app} = 8.1$ we determine the minimum possible Lorentz factor $\gamma_{min} \approx \sqrt{1 + \beta_{app}^2} \approx 8.2$; the viewing angle for $\gamma = \gamma_{min}$ can be estimated by the formula $\theta \approx \sin^{-1}(1/\gamma_{min}) \approx 7^\circ$, and the Doppler boosting factor in this case is close to the value of the Lorentz factor $\delta \approx 8.2$, but it can be much smaller for larger angles (up to $\theta \approx \cos^{-1}(\frac{\beta_{app}^2 - 1}{\beta_{app}^2 + 1}) \approx 14^\circ$) and much larger for smaller angles. For the core outburst (see Fig. 5), the turnover frequency $\nu_m = 37$ GHz and the corresponding flux density $S_m = 1.5$ Jy. The mean elliptical gaussian size of the core from our 43 GHz VLBA data $\Theta_{gm} = (0.085 \pm 0.035)$ mas (Table 3) and the corresponding spherical diameter $\Theta_{sm} = 0.15$ mas. We then obtain for the magnetic field of the core observed at ~ 40 GHz a value $B_{sync} \approx 2.4 (\frac{\delta}{8})$ G. The corresponding time scale in the observer's frame for synchrotron losses of electrons at 37 GHz is $t_{loss} \approx 1.3 B^{-3/2} \nu^{-1/2} (\frac{1+z}{\delta})^{1/2} \approx 0.03 (\frac{\delta}{8})^2$ yr. The shortest timescale of variability observed (from the data shown in Fig. 1) is $t_{var,min} \approx 0.6$ yr (calculated from the formula $t_{var} = (t_2 - t_1) / |\ln(F_2/F_1)|$; Burbidge et al. 1974). Therefore, either the observed timescale corresponds to one of the following: (a) changes in the acceleration rate of relativistic electrons, (b) changes in strength of the magnetic field, or (c) value of the light-travel time across the emitting region, or the magnetic field is lower than the value derived above. This latter possibility would occur if there is substructure within the core: the core is only slightly resolved by our observations and could contain two or more smaller subcomponents. If this is the case, the magnetic field could be as low as $0.3 (\frac{\delta}{8})^{1/3}$ G, which is estimated from the condition $t_{loss} = t_{var,min}$.

Fig. 14 shows that outburst 2 (and probably II) coincides with the moment when jet component *B* goes through the point where the jet changes direction. Therefore, the observed outburst can possibly be explained by a change of viewing angle θ . As has been shown by Marscher et al. (1991) for 4C39.25, even a modest decrease of the viewing angle from the value that gives maximum apparent velocity can result in a flare that is essentially simultaneous at all radio frequencies, while the shock-in-jet model predicts significant delays at low frequencies (Gómez et al. 1997). The flux of component *B* during outburst 2 (see Fig. 16, Table 2) increased by a factor 3. Taking into account that the flux density varies as $S_\nu \propto \delta^{3+\alpha}$, we find that this corresponds to an increase of δ by factor ~ 1.4 , namely from 8.2 to 11, and a decrease in the viewing angle from 7° to 4.4° . The apparent velocity β_{app} in this case should decrease from 8.1 to 7.3 c. Unfortunately, we have no proper motion data for this outburst to check this prediction. If a change in the direction of motion is indeed the cause of the outburst, then future VLBI monitoring should see a change in apparent velocity of superluminal components.

The appearance of a 1.3-yr periodicity, which is especially prominent in the high frequency light curves (see Fig. 7 and Table 1) is interesting. This could be caused, for example, by components passing through periodic compressions and rarefactions in the jet, generated by pressure imbalance with the external medium (e.g., Gómez et al. 1997).

8. Conclusion

We have found a repeated, roughly 4-year cycle of radio variability of the γ -ray quasar 0202+149. We have found also that the start of the 3rd (and last) cycle examined by us coincides with the ejection of an apparent superluminally moving component. If other cycles are similarly related to component ejection, then we have established a regularity (although not a precise periodicity) in the time of ejection. The typical structure of the total flux density variability during the cycle, which was drawn on the basis of the observed cycles, can be explained by the variability of the VLBI core and features in the jet. The first flare of the cycle is caused mainly by an increase in the emission of the VLBI core connected with the ejection of a superluminal component, and the second flare of the cycle is probably caused by a change in the trajectory of the component. The similarity of the cycles of variability can be explained as the result of disturbances flowing down a jet containing a fixed underlying structure. The details of each cycle, such as the amplitude and spectrum, then depends on the strength of the disturbance, while the overall shape of the light curve is roughly the same from one cycle to the next.

If our picture corresponds to reality, then the next ejection of a superluminal component should be in ~ 1998.5 , which should result in an outburst at 37/43 GHz in ~ 1999 , and to an outburst at cm wavelengths about ~ 0.7 year later.

Acknowledgements. We thank T. Clark, C. Ma, and J. Ryan for permission to use data from astrometric and geodetic VLBI-observations, made under the support of NASA (USA). We are grateful to the staff of NASA Goddard Space Flight Center and the National Radio Astronomical Observatory (Socorro) for kind assistance in working with the data. This research has also made use of the United States Naval Observatory (USNO) Radio Reference Frame Image Database (RRFID). The University of Michigan Radio Astronomy Observatory was partially supported by the US National Science Foundation. The Boston University effort was supported in part by U.S. National Science Foundation grant AST-9802941, and by NASA through CGRO Guest Investigator Program grants NAG5-2508, NAG5-3829, and NAG5-7323. The St. Petersburg State University effort was supported in part by the Russian Federal program “Integration”, grant #578, and a grant from the State Committee of Higher Education. The

Institute of Applied Astronomy of the RAS research is supported by Russian Foundation for Basic Research grant 96-02-19177.

References

- Aller H.D., Aller M.F., Latimer G.E., Hodge P.E., 1985, ApJS 59, 513
 Burbidge G.R., Jones T.W., O’Dell S.R., 1974, ApJ 193, 43
 Comastri A., Fossati G., Ghisellini G., Molendi S., 1997, ApJ 480, 534
 Fughmann W., Meisenheimer K., 1988, A&AS 76, 145
 Gómez J.L., Martí J.M., Marscher A.P., Ibáñez J.M., Alberdi A., 1997, ApJ 482, L33
 Hagen-Thorn V.A., Marchenko S.G., Mikolaichuk O.V., Yakovleva V.A., 1997, Astronomy Reports 41, 1
 Herbig T., Readhead A.C.S., 1992, ApJS 81, 83
 Impey C.D., Tapia S., 1990, ApJ 354, 124
 Kellermann K.I., Pauliny-Toth I., 1969, ApJ 115, L71
 Kellermann K.I., Vermeulen R.C., Zensus J.A., Cohen M.H., 1998, AJ 115, 1295
 Krichbaum T.P., Kraus A., Otterbein K., Britzen S., Witzel A., 1998, In: Zensus J.A., Taylor G.B., Wrobel J.M. (eds.) IAU Colloq. 164, Radio Emission from Galactic and Extragalactic Compact Sources. ASP Conf. Ser. 144, p. 37
 Lobanov A.P., 1998, A&A 330, 79
 Marscher A.P., 1987, In: Zensus J.A., Pearson T.J. (eds.) Superluminal Radio Sources. Cambridge Univ. Press, p. 280
 Marscher A.P., Zhang Y.F., Shaffer D.B., Aller H.D., Aller M.F., 1991, ApJ 371, 491
 Mitchel K.J., Dennison B., Condon J.J., et al., 1994, ApJS 93, 441
 Mattox J.R., Schachter J., Molnar L., Hartman R.C., Patnaik A.R., 1997, ApJ 481, 95
 Mutel R.L., Su Bumei, Bucciferro R.R., Phillips R.B., 1990, ApJ 352, 81
 Peacock J.A., Perryman M.A.S., Longair M.S., Gunn J.E., Westphal J.A., 1981, MNRAS 194, 601
 Pyatunina T.B., 1998, In: Proc of the IAU Colloq. no. 164, 157
 Roberts D.H., Lehar J., Dreher J.W., 1987, AJ 93, 968
 Salgado J.F., Altshuler D.R., Gosh T., et al., 1999, ApJS 120, 77
 Shepherd M.C., 1997, In: Astronomical Data Analysis Software and Systems VI, ASP Conf. Ser. 125, p. 77
 Stickel M., Rieke G.H., Kühr H., Rieke M.J., 1996, ApJ 468, 556
 Teräsraanta H., Tornikoski M., Valtaoja E., 1992, A&AS 94, 121
 von Montigny C., Bertsch D.L., Chiang J., et al., 1995, ApJ 440, 525